

Probing nontensorial gravitational waves with a next-generation ground-based detector network

Jierui Hu,¹ Dicong Liang,^{2,*} and Lijing Shao^{2,3,†}

¹*School of Physics, Peking University, Beijing 100871, China*

²*Kavli Institute for Astronomy and Astrophysics, Peking University, Beijing 100871, China*

³*National Astronomical Observatories, Chinese Academy of Sciences, Beijing 100012, China*

(Dated: October 3, 2023)

In General Relativity, there are only two polarizations for gravitational waves. However, up to six polarizations are possible in a generic metric theory of gravity. Therefore, measuring the polarization content of gravitational waves provides an efficient way to test theories of gravity. We analyze the sensitivity of a next-generation ground-based detector network to nontensorial polarizations. We present our method to localize GW signals in the time-frequency domain and construct the null stream for events with known sky locations. We obtain results based on simulations of binary neutron star mergers in a five-detector network. For a single event at a luminosity distance $D_L = 100$ Mpc, the smallest amplitude for detection of scalar and vector modes relative to tensor modes are respectively $A_s = 0.04$ and $A_v = 0.013$. For multiple events in an averaged observing run of 10 years, the detection limits are $A_s = 0.05$ and $A_v = 0.02$. If we are fortunate, a few strong events might significantly improve the limits.

I. INTRODUCTION

Since the first detection of gravitational waves (GWs) in 2015 [1], various tests of gravity are implemented by studying the data from ground-based detectors [2–11]. One of the most important tests is the polarization test. In General Relativity (GR), there are only two tensor modes, namely the plus mode and the cross mode. However, in a generic metric theory of gravity, up to six polarization modes are permitted [12, 13], including two tensor modes, two vector modes (vec-x mode and vec-y mode), and two scalar modes (breathing mode and longitudinal mode). In the Brans-Dicke theory, there is only one extra mode in addition to the tensor modes, which is the breathing mode [12, 13]. While in the $f(R)$ theory and more general scalar-tensor theories, the scalar mode presents in the form of a mixture of the breathing mode and longitudinal mode [14, 15]. The two vector modes appear in many vector-tensor theories [16–19] and the polarization content can be anisotropic when there is a nonzero spatial component in a Lorentz-violating vector background [19–21]. Considering these varieties, searching for extra polarizations that differ from GR in GW signals can be a useful tool to test theories of gravity.

Different methods to search for the existence of extra polarizations in GWs were developed in the literature. Model selection based on Bayesian inference has been applied to compact binary coalescences (CBCs) [22, 23], continuous waves (CWs) [24] and also GW background (GWB) [25, 26]. An alternative method is to remove the tensor polarizations from the data and then check if extra polarizations exist. Null stream, which uses a linear combination of outputs of multiple detectors to

completely eliminate the tensorial GW signals, was proposed to discriminate GW signals from noise glitches in the context of GR [27, 28]. This idea was later extended to the null tests of GR [29, 30] and recently was further developed in Refs. [5, 6, 31–34]. The null stream can be constructed only for one single GW source, while for GWB produced by many sources, one has to make use of the correlation between detectors. Thus, the elimination method is different and the details can be found in Refs. [35–38].

In this paper, we extend the analysis by Pang *et al.* [32] to the next-generation ground-based GW detector network, including Einstein Telescope (ET), Cosmic Explorer (CE), and so on. ET is proposed in Europe, which consists of three co-located detectors with 10 km arm length in a triangular geometry [39]. CE is proposed in America with 40 km arm length in L-shape [40]. The sensitivity of the next-generation detectors, like ET and CE, would have a factor of ten improvement over that of the second-generation detectors [41], which makes them much easier to identify GW signals from the noise background. We develop a new method in Sec. II B to locate the GW signals in the time-frequency domain more accurately. Assuming that tensor modes always present in GW signals, we construct null stream to remove the signals parallel to tensor modes, in order to analyze the extra polarization components. Using the statistical property of the energy of the null stream, we quantify the possibility of the tensor-only hypothesis and estimate the sensitivity of the next-generation GW detector network to extra polarizations.

The paper is structured as follows. We present the method to get the null energy [32] in Sec. II A, and show our method to locate GW signals in time-frequency domain in Sec. II B. Next, we introduce the parameterized form of possible extra polarizations in Sec. II C. Section II D defines the network sensitivity and presents a possible network configuration used in our analysis. The

* Corresponding author: dcliang@pku.edu.cn

† Corresponding author: lishao@pku.edu.cn

simulations of single-event test and multiple-event test are performed in Sec. III, where we quantify the sensitivity to extra polarizations using the relative amplitude. We discuss the results of the relative amplitude sensitivity and compare our multiple-event results with those from the second-generation detector network obtained by Pang *et al.* [32]. Conclusions are drawn in Sec. IV.

II. METHODOLOGY

In this section, we follow Pang *et al.* [32] to present the method to construct the null stream and get the null energy of a GW event with known direction. By using the statistical distribution of the null energy, we assign a p -value to test the extra polarizations in the GW data.

In a generic metric theory of gravity, up to six polarizations are allowed for GWs [12, 13]: two tensor modes (+ and \times), two vector modes (x and y) and two scalar modes (b and l). Thus, the strain of GWs recorded at an interferometric detector can be expressed as a linear combination of these six modes [42],

$$s_{\text{GW}}(t) = \sum_A F^A h_A(t), \quad (1)$$

where $A \in \{+, \times, x, y, b, l\}$ represents the six polarizations, $h_A(t)$ is the strain of polarization A and F^A is its beam pattern function,

$$F^A = D^{ij} e_{ij}^A. \quad (2)$$

In the above equation e_{ij}^A is the polarization tensor and the detector tensor D^{ij} in the low frequency limit is given by [35, 43],

$$D^{ij} = \frac{1}{2}(\hat{u}_i \hat{u}_j - \hat{v}_i \hat{v}_j), \quad (3)$$

where \hat{u} and \hat{v} are the unit vectors of two arms of the detector. Due to the degeneracy between F^b and F^l in the low frequency limit, it is unlikely to distinguish the two scalar modes for the ground-based detectors [35, 43]. Thus, we use breathing mode to represent scalar modes in our analysis.

A. Null energy

Let us consider a network of D interferometric detectors labeled by $j = 0, \dots, D-1$. Here we assume that the GW signals have only tensor modes. The strain data of GW detectors in the frequency domain can be expressed in the following matrix form,

$$\begin{aligned} \tilde{\mathbf{d}}(f) &= \tilde{\mathbf{s}}(f) + \tilde{\mathbf{n}}(f), \\ \tilde{\mathbf{s}}(f) &= \mathbf{F} \tilde{\mathbf{h}}(f), \end{aligned} \quad (4)$$

where

$$\tilde{\mathbf{d}} = \begin{pmatrix} \tilde{d}_0 \\ \vdots \\ \tilde{d}_{D-1} \end{pmatrix}, \quad \tilde{\mathbf{h}} = \begin{pmatrix} \tilde{h}^+ \\ \tilde{h}^\times \end{pmatrix}, \quad \tilde{\mathbf{n}} = \begin{pmatrix} \tilde{n}_0 \\ \vdots \\ \tilde{n}_{D-1} \end{pmatrix}, \quad (5)$$

and

$$\mathbf{F} = (\mathbf{F}^+, \mathbf{F}^\times), \quad (6)$$

$$\mathbf{F}^A = \begin{pmatrix} F_0^A \\ \vdots \\ F_{D-1}^A \end{pmatrix}. \quad (7)$$

Here, we use F_j^A to denote detector j 's beam pattern function for polarization A , and $\mathbf{F} \in \mathbb{R}^{D \times 2}$ is the beam pattern matrix. We further assume that the merger time of the binary in each detector is shifted to be the same.

To facilitate the analysis of signal immersed in the noise, we whiten the data as

$$\tilde{\mathbf{d}}_w(f) = \mathbf{F}_w(f) \tilde{\mathbf{h}}(f) + \tilde{\mathbf{n}}_w(f), \quad (8)$$

where

$$\begin{aligned} \tilde{d}_{w,j}[k] &= \frac{\tilde{d}_j[k]}{\sqrt{S_j[k]/2\Delta f}}, \\ F_{w,j}^A[k] &= \frac{F_j^A}{\sqrt{S_j[k]/2\Delta f}}, \\ \tilde{n}_{w,j}[k] &= \frac{\tilde{n}_j[k]}{\sqrt{S_j[k]/2\Delta f}}. \end{aligned} \quad (9)$$

The subscript w indicates the whitening procedure and $S_j[k]$ is the one-sided power spectral density (PSD) of the noise in detector j at frequency bin k .

For GW sources whose exact sky positions are known from their electromagnetic counterparts, we can project out the tensor components in the GW signal by constructing a null projector for tensor modes,

$$\mathbf{P}_{\text{null}} = \mathbf{I} - \mathbf{F}_w (\mathbf{F}_w^\dagger \mathbf{F}_w)^{-1} \mathbf{F}_w^\dagger, \quad (10)$$

where $\mathbf{F}_w \in \mathbb{R}^{D \times 2}$ only contains beam pattern functions for + and \times modes. Since \mathbf{P}_{null} can project out the tensor signal in Eq. (4), the residue $\tilde{\mathbf{z}}$ after the projection can be written as

$$\tilde{\mathbf{z}} = \mathbf{P}_{\text{null}} \tilde{\mathbf{d}}_w = \mathbf{0} + \mathbf{P}_{\text{null}} \tilde{\mathbf{n}}_w. \quad (11)$$

Notice that, the above projection does not depend on the detailed GW waveform, thus is valid for any tensorial signals. After the projection, the residue only contains noise and that is why it is called *null stream*.

Next, we transform the residue $\tilde{\mathbf{z}}(f)$ back to time domain $\mathbf{z}(t)$ and then perform the normalized Wilson-Daubechies-Meyer (WDM) transform [44] to get the energy distribution in the time-frequency domain,

$$\|\tilde{\mathbf{z}}_{\tau,f}\|^2 = \frac{\left\| \sum_{k \in \mathbb{Z}} e^{i\pi k f / M} \mathbf{z}[\tau M + k] \phi[k] \right\|^2}{\sum_{k \in \mathbb{Z}} \|\phi[k]\|^2}, \quad (12)$$

where τ and f are the time and frequency indices, M is the number of frequency bins and $\phi[k]$ is the window function in the WDM transform. Here we apply the WDM transform because of its superior time-frequency localization capability. The transform is normalized such that each pixel in the time-frequency domain of white noise follows a standard normal distribution. A simple WDM transform written in python can be found online.¹

In general, the signal energy in the gravitational waves from a compact binary coalescence in a circular orbit is encoded in a narrow region in the time-frequency domain. The null projection can wipe out all the energy of the tensorial signals, while it does not affect the statistical property of the noise. From this perspective, it is more sensitive to compare the statistics before and after the null projection for those in the narrow region where the signals locate, instead of the entire region in the time-frequency domain. Fortunately, the next-generation GW detectors have much higher sensitivity than their ancestor generations, which makes it easier to distinguish GW signal pixels from the noise background. It is crucial to apply the process of localizing pixel points to fully utilize the high sensitivity of the next-generation GW detectors. Thus, we only consider the null energy,

$$E_{\text{null}} = \sum_{\tau, f \in S_{\text{GW}}} \|\tilde{z}_{\tau, f}\|^2, \quad (13)$$

where S_{GW} is a set of time-frequency indices that represent the location of the GW signal. If we get the true sky position and there are only tensor modes in the GW signal, the null energy follows a χ^2 distribution with the number of degrees of freedom (DOFs), $n_{\text{DOF}} = N_{\tau f}(D - 2)$, where $N_{\tau f}$ is the number of pixels selected in the time-frequency domain [32].

B. Localizing signal pixels

For a single detector, the signal-to-noise ratio (SNR) of a signal $\tilde{s}(f)$ is defined as

$$\rho = \sqrt{4 \int_0^\infty \frac{\|\tilde{s}(f)\|^2}{S(f)} df}, \quad (14)$$

where $\tilde{s}(f)$ is the observed signal in the frequency domain and $S(f)$ is the one-sided PSD. The network SNR in N detectors is defined as

$$\rho_{\text{net}} = \sqrt{\sum_{j=1}^N \rho_j^2}. \quad (15)$$

When the network SNR is high enough (say, $\rho_{\text{net}} \gtrsim 100$), the GW signal in the time-frequency domain—after

the normalized WDM transform—can be easily identified from the noise background. On one hand, the signal pixels contain a larger power than most noise pixels. On the other hand, the signal pixels are next to each other in the time-frequency plane while the loud noise pixels distribute randomly. Therefore, we devise the following method to select signal pixels in the noisy data.

We use IMRPhenomD_NRTidalv2 waveform model [45] to generate the tensorial signals. The configuration of the detector network is described in detail in Sec. IID. Figure 1 shows an example of localizing pixels for a GW signal from a merger of non-spinning binary neutron star (BNS) with masses $m_1 = m_2 = 1.4 M_\odot$ at a luminosity distance of 450 Mpc. Its network SNR is $\rho_{\text{net}} = 135.8$. The method to select signal pixels is as follows. First, we compute the root mean square normalized WDM transform result from the data of each detector to get the combined WDM transform result, as shown in the left panel of Fig. 1. Second, to represent the GW signal, we select a certain number of the brightest pixels and tag them “good” pixels. However, this procedure might include some loud noise pixels. As an attempt to remove those noise pixels, we only choose the pixels with five or more “good” pixels in the 7 neighbor pixels in the horizontal, vertical, and diagonal directions because, as mentioned earlier, noise pixels are usually less clustered than GW signals. Finally, we obtain the time and frequency indices of the pixels where the GW signals locate, i.e. we obtain the set S_{GW} in Eq. (13), as shown in the right panel of Fig. 1.

Due to the high sensitivity of the next-generation detectors, we will observe the early inspiral of BNS signals. Compared to the late inspiral and the merger stage, the early inspiral lasts for much longer time and the energy encoded in this stage is relatively weaker. Note that including weaker GW data in our analysis may dilute the statistical significance of stronger GW data and is hardly helpful to improve the sensitivity of the test. In practice, we balance the computational efficiency with the length of the data and optimize the number of selected pixels for a better statistical significance. From this perspective, the signal we use in this paper is from the last 32 seconds before merger plus 1 second after merger. Our sampling rate is 1024 Hz.

C. Injection of extra polarizations

Now, let us consider cases where extra polarizations are included in the GW signal. The signal $\tilde{\mathbf{s}}(f)$ in Eq. (4) changes,

$$\tilde{\mathbf{s}}(f) = \mathbf{F}^+ \tilde{h}^+(f) + \mathbf{F}^\times \tilde{h}^\times(f) + \sum_e \mathbf{F}^e \tilde{h}^e(f), \quad (16)$$

where the superscript e denotes extra polarizations $\{x, y, b\}$. The null projector in Eq. (10) can not project out extra polarizations completely, as a consequence, the

¹ <https://github.com/Ecthelion666/WDM-transform-in-python>

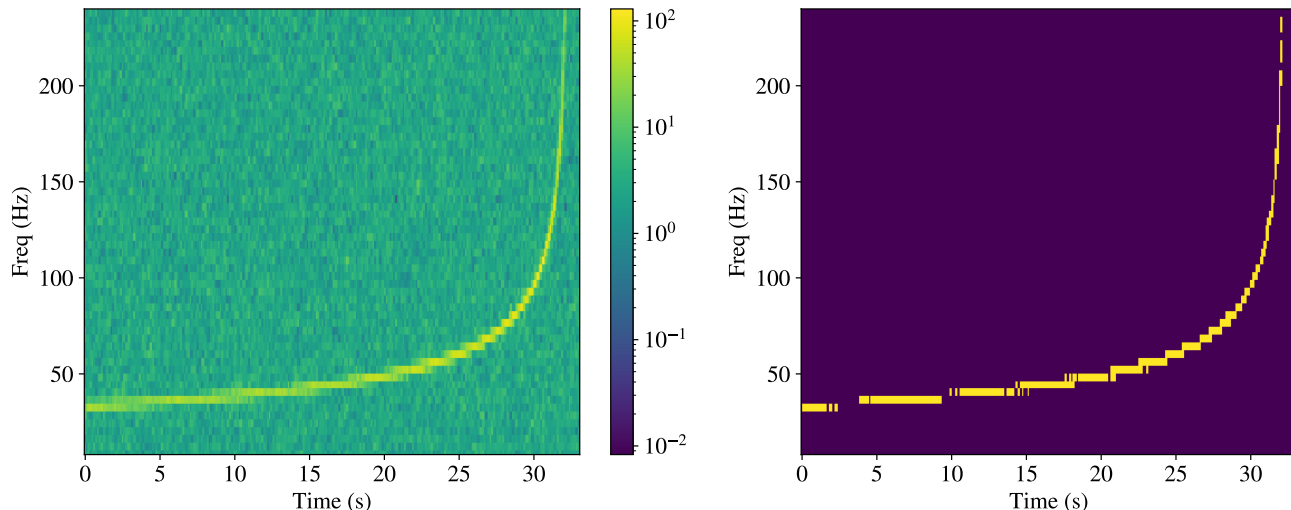


FIG. 1. An example of localizing GW signal. The network SNR is $\rho_{\text{net}} = 135.8$ in this case. The left panel shows the result of the normalized WDM transform, while the right panel shows the pixels that are selected for the polarization test.

residue \tilde{z} becomes

$$\tilde{z} = \mathbf{P}_{\text{null}} \tilde{\mathbf{d}}_w = \mathbf{P}_{\text{null}} \tilde{\mathbf{n}}_w + \sum_e \mathbf{P}_{\text{null}} \mathbf{F}_w^e \tilde{h}^e(f). \quad (17)$$

In general, the introduction of extra polarizations will lead to an increase in the expected value of the null energy, comparing to the noise-only data. Therefore, the null energy calculated by Eq. (13) no longer follows the χ^2 distribution, and can be used as a statistic to quantify the significance of extra polarizations.

To test the sensitivity of next-generation GW detectors to extra polarizations, we inject scalar and vector modes into the GW signal separately. For simplicity, we use $\mathbf{F}^b \in \mathbb{R}^{D \times 1}$ as the beam pattern function for the scalar mode because of the degeneracy between the response of breathing mode and longitudinal mode. Furthermore, We assume that the scalar modes are proportional to the plus mode with a relative amplitude A_s , which can be interpreted as combining both the inclination dependence of the scalar mode and the relative strength between the scalar component and the tensorial component h^+ in a specific gravity theory [46]. Hence, the scalar mode can be expressed as

$$\tilde{\mathbf{s}}_s(f) = \mathbf{F}^b A_s \tilde{h}^+(f). \quad (18)$$

Similarly, we generate the two vector modes from the two tensor modes with a relative amplitude A_v ,

$$\tilde{\mathbf{s}}_v(f) = \mathbf{F}^x A_v \tilde{h}^+(f) + \mathbf{F}^y A_v \tilde{h}^\times(f). \quad (19)$$

Here we have assumed specific proportionalities for the x and y vector modes. It is easy to release these assumptions.

As we know, in some modified gravity theories, extra polarizations might have different frequency evolution behaviours from the tensor modes, thus they introduce multiple harmonics [29, 47–49]. To test the existence of such

harmonics, we do not need to apply the null projector to get the null energy because there is a clear distinction in the location for different harmonics in the time-frequency plane. We can use the frequency evolution between different harmonics to localize extra polarization components and then check if there is any significant excess of energy. The methodology is similar and we will not discuss these cases here. In general, these are easier to search for as GW data analysis is more sensitive to phase evolution. When the extra polarizations have the same frequency evolution as the tensor polarizations, they overlap with each other in the time-frequency domain. Then we have to use the null projection to remove the tensorial component. In this sense, the cases studied in this work is conservative.

For GW events with known sky position, we can get the null energy using Eq. (13) and assign a p -value to the tensor-only hypothesis,

$$p = \int_{E_{\text{null}}}^{\infty} \chi_{\text{DOF}}^2(x) dx. \quad (20)$$

Under this null hypothesis, p is uniformly distributed between 0 and 1. After injecting a non-zero extra polarization signal like in Eq. (18) or Eq. (19), the distribution of p will deviate from the null hypothesis because the presence of extra polarizations will enlarge the null energy. Therefore, a small p -value suggests a deviation from GR. In this work, we mainly use this p -value to evaluate the sensitivity of a next-generation detector network to extra polarizations.

TABLE I. Geometric angles for GW detectors in a network.

Facility	Λ	λ	γ	ζ
CE (Hanford)	46°455	-119°408	278°979	90°
CE (Livingston)	30°563	-90°774	207°280	90°
CE (Southeastern Australia)	-35°000	148°000	272°450	90°
ET (Maastricht)	50°754	6°025	247°761	60°
ET (Maastricht)	50°754	6°025	127°761	60°

D. GW detector network sensitivity

Now we present the configuration of a next-generation GW detector network used in this work. After that we introduce the optimal network sensitivity to extra polarizations.

We define the optimal network sensitivity $\alpha^A(f, \hat{\Omega})$ before and after applying the null projection for polarization mode A as

$$\alpha_{\text{before}}^A(f, \hat{\Omega}) = |\mathbf{F}_w^A(f)|, \quad (21)$$

$$\alpha_{\text{after}}^A(f, \hat{\Omega}) = |\mathbf{P}_{\text{null}}(f)\mathbf{F}_w^A(f)|. \quad (22)$$

Both $\alpha_{\text{before}}^A(f, \hat{\Omega})$ and $\alpha_{\text{after}}^A(f, \hat{\Omega})$ are functions of the sky position $\hat{\Omega}$ because $\mathbf{P}_{\text{null}}(f)$ and $\mathbf{F}_w^A(f)$ are functions of $\hat{\Omega}$. The optimal network sensitivities to scalar modes, vector modes and tensor modes are defined as

$$\begin{aligned} \alpha^{\text{Scalar}}(f, \hat{\Omega}) &= \alpha^b(f, \hat{\Omega}), \\ \alpha^{\text{Vector}}(f, \hat{\Omega}) &= \sqrt{[\alpha^x(f, \hat{\Omega})]^2 + [\alpha^y(f, \hat{\Omega})]^2}, \\ \alpha^{\text{Tensor}}(f, \hat{\Omega}) &= \sqrt{[\alpha^+(f, \hat{\Omega})]^2 + [\alpha^\times(f, \hat{\Omega})]^2}. \end{aligned} \quad (23)$$

In this paper, we consider a GW detector network, “2ET+3CE”, consists of two pairs of ET-like detectors (namely two interferometric detectors with one arm overlapping with each other) located at Maastricht in the Netherlands, and three CE-like detectors located respectively at Hanford and Livingston in the America, and Southeastern Australia. Table I gives the geometric factors (latitude Λ , longitude λ , bisector angle γ and opening angle ζ between detector’s arms) of this detector network. The azimuths are defined as clockwise relative to the due North.

For the sensitivities of CE-like and ET-like detectors, we use two analytical PSDs, CosmicExplorerP1600143 and EinsteinTelescopeP1600143, in the PyCBC package [50]. Figure 2 shows the normalized optimal network sensitivity sky maps of the “2ET+3CE” network at 100 Hz. For each polarization mode, we normalize the sensitivity values such that the maximum value of the optimal sensitivity before projection is unity. The normalization factors are,

$$\alpha_{\text{before,max}}^{\text{Scalar}} = 1.83 \times 10^{24}, \quad (24)$$

$$\alpha_{\text{before,max}}^{\text{Vector}} = 3.60 \times 10^{24}, \quad (25)$$

$$\alpha_{\text{before,max}}^{\text{Tensor}} = 3.49 \times 10^{24}. \quad (26)$$

From Fig. 2, we can see that the tensor modes are completely projected out as expected and the sensitivity to the extra modes is also deteriorated. Besides, there are more residuals in vector modes after projection than in scalar modes because the detectors’ response of the vector modes has less overlap with that of the tensor modes.

As we will see in the next section, $\alpha_{\text{after}}^A(f, \hat{\Omega})$ can serve as a computationally efficient indicator of the detectors’ sensitivity to extra polarizations and can be used as a guidance for optimizing future detector network configuration for extra polarization searches.

III. RESULTS AND DISCUSSIONS

With the methodology presented above, we give our results for single events in Sec. III A and for multiple events in Sec. III B.

A. Single events

If the signal of extra polarization is very strong and there remains enough energy after the null projection, then we can get an extremely small p -value in a loud GW event. By setting the threshold p -value to $p = 10^{-5}$, we want to estimate the minimum relative amplitude A_s or A_v —that we call *relative amplitude sensitivity*—in different sky position. When the actual relative amplitude of the additional polarization components in the GW signal is greater than the relative amplitude sensitivity, we are likely to confirm the existence of extra polarizations in a single event. Here we consider a BNS with masses $m_1 = m_2 = 1.4 M_\odot$ and at a luminosity distance $D_L = 100$ Mpc for this study.

The left panels in Fig. 3 show the relative amplitude sensitivity sky map of the “2ET+3CE” network, and the right panels show the distribution of the relative amplitude sensitivity. The minimum relative amplitude sensitivities for scalar modes and vector modes are,

$$A_{s,\text{min}} = 0.043, \quad (p\text{-value} = 10^{-5}), \quad (27)$$

$$A_{v,\text{min}} = 0.013, \quad (p\text{-value} = 10^{-5}). \quad (28)$$

The mean values are,

$$A_{s,\text{mean}} = 0.132, \quad (p\text{-value} = 10^{-5}), \quad (29)$$

$$A_{v,\text{mean}} = 0.041, \quad (p\text{-value} = 10^{-5}). \quad (30)$$

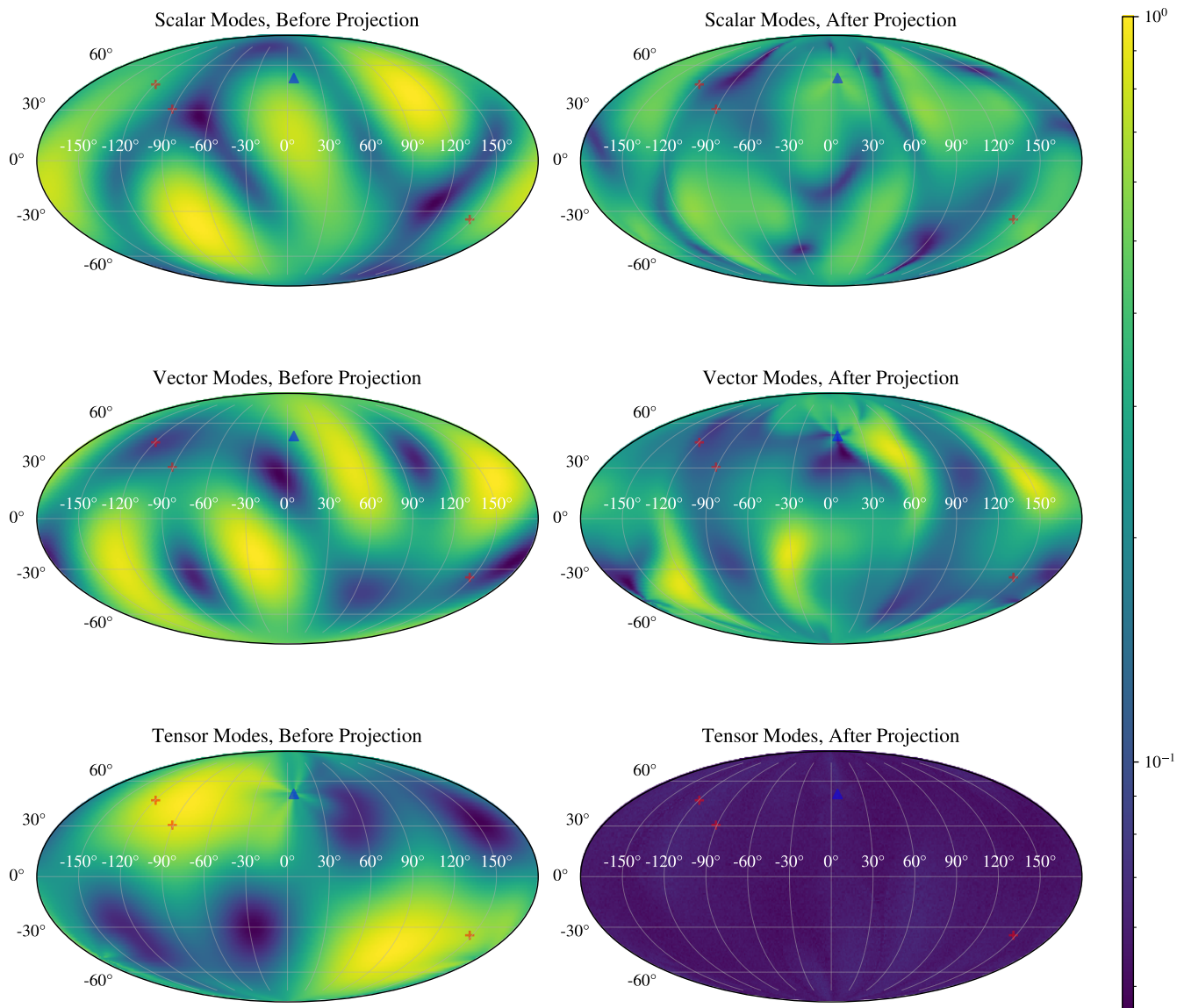


FIG. 2. Normalized sky maps of optimal network sensitivity at 100 Hz. The blue Δ is the location of the pair of ET-like detectors, and the red $+$ signs stand for three CE-like detectors. The plots in each polarization category are normalized by the maximum value of the optimal network sensitivity before projection, which means that the maximum values of the left panels are 1. The normalization factors are given in Eqs. (24–26).

The relative amplitudes of vector modes are smaller than scalar modes for two reasons. First, there is one more component in the vector modes [see Eq. (19)] than scalar modes [see Eq. (18)]. Second, the vector modes have more residuals than the scalar mode after applying the null projection (see the right panels in Fig. 2).

We can see that the pattern of scalar and vector modes in the sky maps of the right panels in Fig. 2 is similar to the sky maps in Fig. 3. This is because the null energy is proportional to the square of $\alpha_{\text{after}}^A(f, \hat{\Omega})$ and the p -value is negatively correlated to the null energy. Hence, the optimal sensitivity $\alpha_{\text{after}}^A(f, \hat{\Omega})$ can be used to roughly estimate the relative amplitude sensitivity, and

these two quantities are negatively correlated. It is worth noting that the choice of frequency in $\alpha_{\text{after}}^A(f, \hat{\Omega})$ does not have a large impact on the result because the PSD of the five detectors has similar shape in the sensitive frequency band.

B. Multiple events

If the result in a single event is not significant enough to decide the existence of extra polarizations, we can accumulate multiple GW events to perform a combined analysis. In this subsection we present simulations of multiple

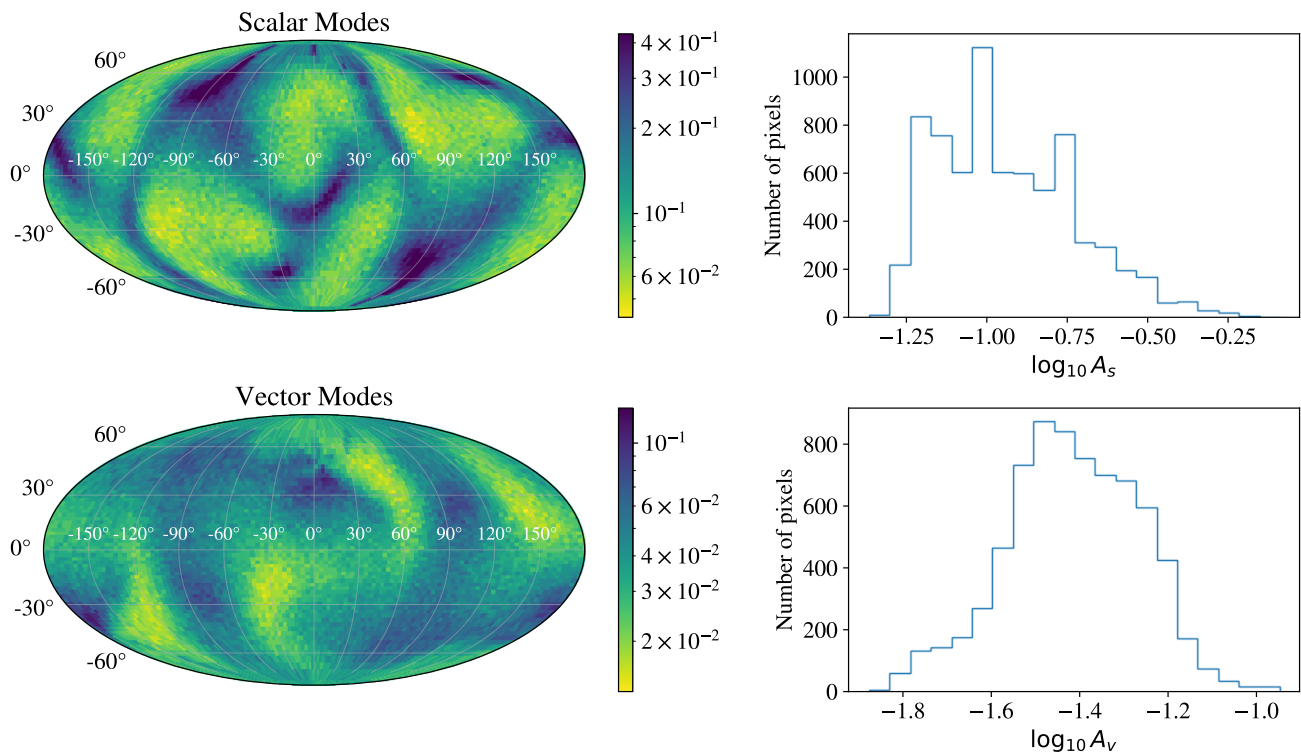


FIG. 3. The left panels show the relative amplitude sensitivity sky maps for scalar modes and vector modes, where the relative amplitude sensitivity is defined as the minimum A_s or A_v in sky position $\hat{\Omega}$ to achieve $p < 10^{-5}$. The resolution of the event's sky location is 120 pixels in longitude and 60 pixels in latitude, and each pixel has a same solid angle. The histograms on the right are the distribution of the minimum relative amplitudes. The minimum relative amplitude sensitivities for scalar modes and vector modes are given in Eqs. (27–28) and the mean values are given in Eqs. (29–30).

events, which give a combined result from a long observing period.

As shown in Appendix A, if the p -value of a single event i , p_i , is uniformly distributed between 0 and 1, the statistic S given by

$$S = -2 \sum_{i=1}^N \log p_i \quad (31)$$

follows a χ^2 distribution with $n_{\text{DOF}} = 2N$. Therefore, the combined p -value, p_{com} , can be defined as

$$p_{\text{com}} = \int_S^{\infty} \chi_{2N}^2(x) dx, \quad (32)$$

which characterizes the sensitivity of multiple events to extra polarizations.

In this multiple-event study, we generate GW events of BNSs randomly distributed within a sphere that has a large radius with a luminosity distance $D_L \leq 1 \text{ Gpc}$. The masses of the neutron stars are simply assumed to be $1.4 M_{\odot}$. In reality, the mass of neutron stars has a relatively narrow distribution compared to black holes, and it does not change significantly the SNR of signals. As we can see in Figs. 2 and 3, the sky location affects

the sensitivity of the test significantly, and the difference can be as large as one order of magnitude. Therefore, our treatment to BNS masses suffice for this study and can be extended in more dedicated studies in the future. In our test, we only select sources whose $\rho_{\text{net}} > 350$ (within a radius $D_L \lesssim 200 \text{ Mpc}$ approximately) to calculate p_{com} and these sources account for $\sim 1\%$ of the total sources in our simulations. The events with lower SNRs are discarded from this analysis.

Figure 4 shows the quantity $\log_{10} p_{\text{com}}$ against the number of combined events, averaged over 100 simulations. In our simulation, when the merger rate of BNSs is chosen to be $1000 \text{ Gpc}^{-3} \text{ yr}^{-1}$, it will take about 10 years to generate about 100 candidate events with $\rho_{\text{net}} > 350$. With such an event rate, it would take about 5 years for $A_s = 0.06$ and 3 years for $A_v = 0.03$ to reach the $5\text{-}\sigma$ criterion. When the relative amplitude gets smaller, it would take more time for p_{com} to hit the $5\text{-}\sigma$ line. The most recent inferred BNS merger rate is between 10 and $1700 \text{ Gpc}^{-3} \text{ yr}^{-1}$ [51]. Since the GW sources that we analyzed are close enough, we can simply rescale the time scale according to the realistic merger rate.

We note that in Fig. 4 there are some steep declines in the brown lines in both panels ($A_s = 0.06$ for the scalar mode and $A_v = 0.03$ for the vector modes). This

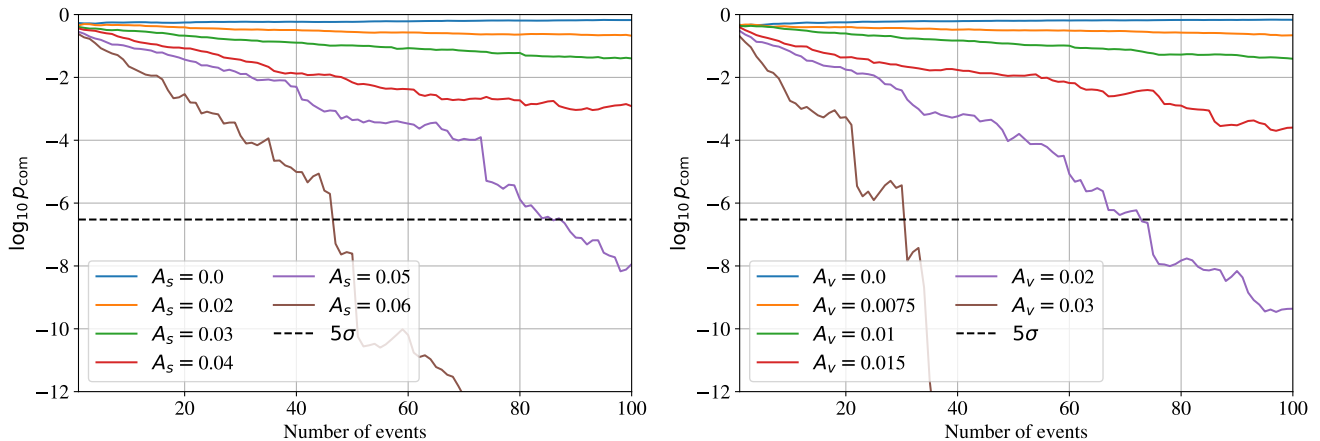


FIG. 4. Combined p -value against the number of BNS events with $\rho_{\text{net}} > 350$. Each line denotes a different relative ρ amplitude for scalar modes (left) or vector modes (right). The horizontal dashed line is the $5\text{-}\sigma$ criterion.

is attributed to some rare events with small distances at specific sky locations. As we can see in Sec. III A, the p -value of a single event at $D_L = 100$ Mpc might reach 10^{-5} when the relative amplitude is $A_{s,\text{min}} = 0.043$ or $A_{v,\text{min}} = 0.013$. In practice, the significant contribution to the p -value from a single strong signal may outweigh dozens of weaker signals.

For the multiple-event test by Pang *et al.* [32], the combined p -value of the null hypothesis declines monotonically with the increasing numbers of GW events. It suggests that when the detection number is large enough, we cannot tell apart the reason for an extremely small p_{com} value, either due to extra polarizations or the defects of the null-stream method. While in our simulations, the p_{com} value does not decrease monotonically, but instead it is relatively stable after accumulating a large number of events. This is attributed to the high sensitivity of the next-generation detectors, which allow us to locate the GW signals more precisely while avoiding mistakenly selecting the noise pixels.

Notice that, the above p -value analysis can only indicate the existence of extra polarizations, but cannot tell which extra polarizations are present in the signals. Theoretically, it is possible to solve the equations, $\tilde{\mathbf{d}}(f) = \mathbf{F}\tilde{\mathbf{h}}(f) + \tilde{\mathbf{n}}(f)$, to test extra polarizations when we have five non-degenerate detectors. This is because that, due to the degenerate response of GW detectors to the breathing mode and the longitudinal mode, there are only five independent responses to all possible polarizations. Such a study is out of the scope of this work and we leave it to the future.

IV. CONCLUSIONS

In this work, we utilize the null stream to test the detectability of extra polarizations in GWs with a next-

generation detector network. We introduce an approach to improve the sensitivity of the test by locating GW signals in the time-frequency domain precisely, though the exact sky locations of the GW signals are needed to do so. Using the high sensitivity of the next-generation GW detectors, we can circumvent the influence of loud noise pixels to get a more robust result, by looking for possible deviations via the p -value for the null hypothesis that there are only two tensorial modes. It improves the method presented by Pang *et al.* [32].

We use a detector network consisting of two ET-like detectors and three CE-like detectors for illustrative purposes. We estimate the sensitivity of this network for GW events coming from different sky positions by computing the network sensitivity in Eq. (22). It also provides guidance for optimizing the geometry of GW detectors for extra polarizations. We simulate signals with extra polarizations and get the detection thresholds for relative amplitudes, which are $A_{s,\text{min}} = 0.043$ for the scalar mode and $A_{v,\text{min}} = 0.013$ for vector modes, for a single BNS event at a luminosity distance $D_L = 100$ Mpc in an optimal sky location. Finally, we combined the results from multiple events. For a 10-year observation with BNS events uniformly distributed in the local Universe with an event rate of $1000\text{yr}^{-1}\text{Gpc}^{-3}$, the averaged results indicate that the detection limits of relative amplitudes are $A_{s,\text{min}} \simeq 0.05$ for the scalar mode and $A_{v,\text{min}} \simeq 0.02$ for the vector modes. However, if we are fortunate enough to observe some golden BNS events in the observing run, this limit might become much better.

Note that the sky positions are assumed to be known in our analysis, but in practice the uncertainty of the sky positions can make the p -value smaller even for the null hypothesis. Nevertheless, we rely on future electromagnetic instruments to precisely locate nearby BNS events [52].

ACKNOWLEDGMENTS

We thank Yacheng Kang for helpful discussions. This work was supported by the National Natural Science Foundation of China (11975027, 11991053), the China Postdoctoral Science Foundation (2021TQ0018), the National SKA Program of China (2020SKA0120300), the Max Planck Partner Group Program funded by the Max Planck Society, and the High-Performance Computing Platform of Peking University. J.H. was supported by the National Training Program of Innovation for Undergraduates at Peking University.

Appendix A: The statistic S

To prove the statistic S in Eq. (31) follows a χ^2 distribution with $n_{\text{DOF}} = 2N$, it is sufficient to prove that each $-2 \log p_i$ term in Eq. (31) follows a χ^2 distribution with 2

DOFs. It is known that each p_i is uniformly distributed in $[0, 1]$.

Let us define Y as

$$Y = -2 \log p. \quad (\text{A1})$$

The probability density of Y is $D(Y)$, which satisfies

$$D(Y)dY = D(p)dp, \quad (\text{A2})$$

and $D(p) = 1$ is the probability density of p . The solution to Eq. (A2) is

$$D(Y) = \frac{1}{2} e^{-\frac{Y}{2}}, \quad (\text{A3})$$

which is the probability density of a χ^2 distribution with 2 DOFs. Because each p_i in Eq. (31) is independent to each other, the sum of $-2 \log(p_i)$ follows a χ^2 distribution with $2N$ DOFs.

-
- [1] B. P. Abbott *et al.* (LIGO Scientific, Virgo), *Phys. Rev. Lett.* **116**, 061102 (2016), [arXiv:1602.03837 \[gr-qc\]](#).
- [2] B. P. Abbott *et al.* (LIGO Scientific, Virgo), *Phys. Rev. Lett.* **116**, 221101 (2016), [Erratum: *Phys.Rev.Lett.* 121, 129902 (2018)], [arXiv:1602.03841 \[gr-qc\]](#).
- [3] B. P. Abbott *et al.* (LIGO Scientific, Virgo), *Phys. Rev. Lett.* **123**, 011102 (2019), [arXiv:1811.00364 \[gr-qc\]](#).
- [4] B. P. Abbott *et al.* (LIGO Scientific, Virgo), *Phys. Rev. D* **100**, 104036 (2019), [arXiv:1903.04467 \[gr-qc\]](#).
- [5] R. Abbott *et al.* (LIGO Scientific, Virgo), *Phys. Rev. D* **103**, 122002 (2021), [arXiv:2010.14529 \[gr-qc\]](#).
- [6] R. Abbott *et al.* (LIGO Scientific, VIRGO, KAGRA), (2021), [arXiv:2112.06861 \[gr-qc\]](#).
- [7] N. Yunes, K. Yagi, and F. Pretorius, *Phys. Rev. D* **94**, 084002 (2016), [arXiv:1603.08955 \[gr-qc\]](#).
- [8] E. Berti, K. Yagi, and N. Yunes, *Gen. Rel. Grav.* **50**, 46 (2018), [arXiv:1801.03208 \[gr-qc\]](#).
- [9] E. Berti, K. Yagi, H. Yang, and N. Yunes, *Gen. Rel. Grav.* **50**, 49 (2018), [arXiv:1801.03587 \[gr-qc\]](#).
- [10] B. Sathyaprakash *et al.*, *Bull. Am. Astron. Soc.* **51**, 251 (2019), [arXiv:1903.09221 \[astro-ph.HE\]](#).
- [11] V. Kalogera *et al.*, (2021), [arXiv:2111.06990 \[gr-qc\]](#).
- [12] D. M. Eardley, D. L. Lee, and A. P. Lightman, *Phys. Rev. D* **8**, 3308 (1973).
- [13] D. M. Eardley, D. L. Lee, A. P. Lightman, R. V. Wagoner, and C. M. Will, *Phys. Rev. Lett.* **30**, 884 (1973).
- [14] S. Hou, Y. Gong, and Y. Liu, *Eur. Phys. J. C* **78**, 378 (2018), [arXiv:1704.01899 \[gr-qc\]](#).
- [15] D. Liang, Y. Gong, S. Hou, and Y. Liu, *Phys. Rev. D* **95**, 104034 (2017), [arXiv:1701.05998 \[gr-qc\]](#).
- [16] T. Jacobson and D. Mattingly, *Phys. Rev. D* **70**, 024003 (2004), [arXiv:gr-qc/0402005](#).
- [17] Y. Gong, S. Hou, D. Liang, and E. Papantonopoulos, *Phys. Rev. D* **97**, 084040 (2018), [arXiv:1801.03382 \[gr-qc\]](#).
- [18] Y.-Q. Dong, Y.-Q. Liu, and Y.-X. Liu, (2023), [arXiv:2305.12516 \[gr-qc\]](#).
- [19] D. Liang, R. Xu, X. Lu, and L. Shao, *Phys. Rev. D* **106**, 124019 (2022), [arXiv:2207.14423 \[gr-qc\]](#).
- [20] V. A. Kostelecký, *Phys. Rev. D* **69**, 105009 (2004), [arXiv:hep-th/0312310](#).
- [21] Q. G. Bailey, A. S. Gard, N. A. Nilsson, R. Xu, and L. Shao, (2023), [arXiv:2307.13374 \[gr-qc\]](#).
- [22] M. Isi and A. J. Weinstein, (2017), [arXiv:1710.03794 \[gr-qc\]](#).
- [23] B. P. Abbott *et al.* (LIGO Scientific, Virgo), *Phys. Rev. Lett.* **119**, 141101 (2017), [arXiv:1709.09660 \[gr-qc\]](#).
- [24] M. Isi, M. Pitkin, and A. J. Weinstein, *Phys. Rev. D* **96**, 042001 (2017), [arXiv:1703.07530 \[gr-qc\]](#).
- [25] T. Callister, A. S. Biscoveanu, N. Christensen, M. Isi, A. Matas, O. Minazzoli, T. Regimbau, M. Sakellariadou, J. Tasson, and E. Thrane, *Phys. Rev. X* **7**, 041058 (2017), [arXiv:1704.08373 \[gr-qc\]](#).
- [26] B. P. Abbott *et al.* (LIGO Scientific, Virgo), *Phys. Rev. Lett.* **120**, 201102 (2018), [arXiv:1802.10194 \[gr-qc\]](#).
- [27] Y. Guersel and M. Tinto, *Phys. Rev. D* **40**, 3884 (1989).
- [28] S. Chatteerji, A. Lazzarini, L. Stein, P. J. Sutton, A. Searle, and M. Tinto, *Phys. Rev. D* **74**, 082005 (2006), [arXiv:gr-qc/0605002](#).
- [29] K. Chatziioannou, N. Yunes, and N. Cornish, *Phys. Rev. D* **86**, 022004 (2012), [Erratum: *Phys.Rev.D* 95, 129901 (2017)], [arXiv:1204.2585 \[gr-qc\]](#).
- [30] K. Hayama and A. Nishizawa, *Phys. Rev. D* **87**, 062003 (2013), [arXiv:1208.4596 \[gr-qc\]](#).
- [31] Y. Hagihara, N. Era, D. Iikawa, A. Nishizawa, and H. Asada, *Phys. Rev. D* **100**, 064010 (2019), [arXiv:1904.02300 \[gr-qc\]](#).
- [32] P. T. H. Pang, R. K. L. Lo, I. C. F. Wong, T. G. F. Li, and C. Van Den Broeck, *Phys. Rev. D* **101**, 104055 (2020), [arXiv:2003.07375 \[gr-qc\]](#).
- [33] I. C. F. Wong, P. T. H. Pang, R. K. L. Lo, T. G. F. Li, and C. Van Den Broeck, (2021), [arXiv:2105.09485 \[gr-qc\]](#).
- [34] C. Zhang, Y. Gong, D. Liang, and C. Zhang, *Phys. Rev. D* **105**, 104062 (2022), [arXiv:2102.03972 \[gr-qc\]](#).
- [35] A. Nishizawa, A. Taruya, K. Hayama, S. Kawamura,

- and M.-a. Sakagami, *Phys. Rev. D* **79**, 082002 (2009), [arXiv:0903.0528 \[astro-ph.CO\]](#).
- [36] A. Nishizawa, A. Taruya, and S. Kawamura, *Phys. Rev. D* **81**, 104043 (2010), [arXiv:0911.0525 \[gr-qc\]](#).
- [37] H. Omiya and N. Seto, *Phys. Rev. D* **102**, 084053 (2020), [arXiv:2010.00771 \[gr-qc\]](#).
- [38] L. Amalberti, N. Bartolo, and A. Ricciardone, *Phys. Rev. D* **105**, 064033 (2022), [arXiv:2105.13197 \[astro-ph.CO\]](#).
- [39] M. Punturo *et al.*, *Class. Quant. Grav.* **27**, 194002 (2010).
- [40] D. Reitze *et al.*, *Bull. Am. Astron. Soc.* **51**, 035 (2019), [arXiv:1907.04833 \[astro-ph.IM\]](#).
- [41] B. P. Abbott *et al.* (LIGO Scientific), *Class. Quant. Grav.* **34**, 044001 (2017), [arXiv:1607.08697 \[astro-ph.IM\]](#).
- [42] C. M. Will, *Living Rev. Rel.* **17**, 4 (2014), [arXiv:1403.7377 \[gr-qc\]](#).
- [43] D. Liang, Y. Gong, A. J. Weinstein, C. Zhang, and C. Zhang, *Phys. Rev. D* **99**, 104027 (2019), [arXiv:1901.09624 \[gr-qc\]](#).
- [44] V. Nucea, S. Klimenko, and G. Mitselmakher, *J. Phys. Conf. Ser.* **363**, 012032 (2012).
- [45] T. Dietrich, A. Samajdar, S. Khan, N. K. Johnson-McDaniel, R. Dudi, and W. Tichy, *Phys. Rev. D* **100**, 044003 (2019), [arXiv:1905.06011 \[gr-qc\]](#).
- [46] H. Takeda, A. Nishizawa, Y. Michimura, K. Nagano, K. Komori, M. Ando, and K. Hayama, *Phys. Rev. D* **98**, 022008 (2018).
- [47] C. Zhang, X. Zhao, A. Wang, B. Wang, K. Yagi, N. Yunes, W. Zhao, and T. Zhu, *Phys. Rev. D* **101**, 044002 (2020), [Erratum: *Phys.Rev.D* 104, 069905 (2021)], [arXiv:1911.10278 \[gr-qc\]](#).
- [48] T. Liu, W. Zhao, and Y. Wang, *Phys. Rev. D* **102**, 124035 (2020), [arXiv:2007.10068 \[gr-qc\]](#).
- [49] Y. Higashino and S. Tsujikawa, *Phys. Rev. D* **107**, 044003 (2023), [arXiv:2209.13749 \[gr-qc\]](#).
- [50] S. A. Usman *et al.*, *Class. Quant. Grav.* **33**, 215004 (2016), [arXiv:1508.02357 \[gr-qc\]](#).
- [51] R. Abbott *et al.* (KAGRA, VIRGO, LIGO Scientific), *Phys. Rev. X* **13**, 011048 (2023), [arXiv:2111.03634 \[astro-ph.HE\]](#).
- [52] B. P. Abbott *et al.* (KAGRA, LIGO Scientific, Virgo, VIRGO), *Living Rev. Rel.* **21**, 3 (2018), [arXiv:1304.0670 \[gr-qc\]](#).